

Small molecule-assisted synthesis of carbon supported platinum intermetallic fuel cell catalysts

Received: 7 June 2022

Accepted: 12 October 2022

Published online: 31 October 2022

Check for updates

Tian-Wei Song¹, Cong Xu¹, Zhu-Tao Sheng², Hui-Kun Yan¹, Lei Tong¹, Jun Liu^{3,4}, Wei-Jie Zeng¹, Lu-Jie Zuo¹, Peng Yin¹, Ming Zuo¹, Sheng-Qi Chu⁵, Ping Chen⁶ & Hai-Wei Liang¹✉

Supported ordered intermetallic compounds exhibit superior catalytic performance over their disordered alloy counterparts in diverse reactions. But the synthesis of intermetallic compounds catalysts often requires high-temperature annealing that leads to the sintering of metals into larger crystallites. Herein, we report a small molecule-assisted impregnation approach to realize the general synthesis of a family of intermetallic catalysts, consisting of 18 binary platinum intermetallic compounds supported on carbon blacks. The molecular additives containing heteroatoms (that is, O, N, or S) can be coordinated with platinum in impregnation and thermally converted into heteroatom-doped graphene layers in high-temperature annealing, which significantly suppress alloy sintering and insure the formation of small-sized intermetallic catalysts. The prepared optimal PtCo intermetallics as cathodic oxygen-reduction catalysts exhibit a high mass activity of 1.08 A mg_{Pt}⁻¹ at 0.9 V in H₂-O₂ fuel cells and a rated power density of 1.17 W cm⁻² in H₂-air fuel cells.

Intermetallic compounds (IMCs), as a special kind of alloy materials with heterometallic bonding, defined stoichiometry, and long-range atomically ordered crystal structure, have raised sustained research interests in diverse catalytic fields including chemical transformations, organic synthesis, gas purification, and energy conversion^{1–3}. Particularly, carbon supported Pt-M (M is a base metal, typically a 3d transition metal) IMCs represent one of the most promising low-Pt electrocatalysts for the sluggish oxygen-reduction reaction (ORR)^{4–6}, a bottleneck restricting the large-scale commercialization of proton-exchange-membrane fuel cells (PEMFCs) vehicles. For catalyzing ORR, Pt-IMCs catalysts are distinctly advantageous over their disordered counterparts in activity enhancement, which can be ascribed to the more pronounced ligand and/or strain effects in ordered IMCs structures^{7–12}. Moreover, the strong 3d–5d orbital interactions between M and Pt lead to a larger formation enthalpy in IMCs relative to

disordered alloys, resulting in enhanced structural stability of the IMCs catalysts under corrosive fuel cell conditions^{13,14}.

In thermodynamics, the Gibbs' free energy ($\Delta G_{d \rightarrow o}^\infty$) change in disorder-to-order phase-transition depends on the temperature (T), the change of enthalpy ($\Delta H_{d \rightarrow o}$), and the entropy ($\Delta S_{d \rightarrow o}$)¹⁵:

$$\Delta G_{d \rightarrow o}^\infty = \Delta H_{d \rightarrow o} - T \Delta S_{d \rightarrow o} \quad (1)$$

where d and o indicate the disordered and ordered structures, respectively. The stronger Pt-M heterometallic bonding energy in ordered structures relative to disordered ones makes $\Delta H_{d \rightarrow o}$ negative, while $\Delta S_{d \rightarrow o}$ is also negative in the atom ordering process. Accordingly, the ordered intermetallics are thermodynamically favorable to generate relative to disordered solid solutions below the phase-transition temperature. In kinetics, the realization of the disorder-to-

¹Hefei National Research Center for Physical Sciences at the Microscale, Department of Chemistry, University of Science and Technology of China, Hefei 230026, China. ²College of Chemistry and Materials Science, Anhui Normal University, Wuhu 241000, China. ³Institute of Solid State Physics, Hefei Institutes of Physical Science, Chinese Academy of Sciences, Hefei 230031, China. ⁴Anhui Contango New Energy Technology Co., Ltd, Hefei 230088, China. ⁵Institute of High Energy Physics, Chinese Academy of Sciences, Beijing 100049, China. ⁶School of Chemistry and Chemical Engineering, Anhui University, Hefei 230601, China. ✉e-mail: hwliang@ustc.edu.cn

order transition, however, must overcome the high energy barrier of atom diffusion and ordering in solid states. Although direct low-temperature solution syntheses and electrochemical methods are effective for preparing a few low-melting-point Pt and Pd-based intermetallics^{9,16–18}, the synthesis of most Pt-IMCs catalysts generally requires a high-temperature thermal annealing process to promote atomic ordering, which inevitably leads to metal sintering and makes it challenging to produce nano-sized IMCs catalysts with high surface areas and mass-based activities for practical applications^{5,19,20}.

Recent efforts aimed at preparing small Pt-IMCs nanoparticle catalysts, particularly for fuel cell application^{5,21–26}, include coating disordered alloy nanoparticles with carbons or metal oxide protective shells prior to high-temperature annealing^{27–31}, KCl matrix-assisted annealing³², heteroatom-doped carbons anchoring synthesis^{6,33}, low-temperature chemical vapor deposition with organometallic precursors³⁴, and thermal decomposition of heterometallic compound precursors³⁵. Yet, despite these efforts, a more effective method needs to be developed to break the trade-off between small particle size (thus high electrochemically active surface areas) and high ordering degree of Pt intermetallic catalysts for the further PEMFCs performance improvement^{36,37}.

Here, we develop a small molecule-assisted impregnation approach to realize the grams scale synthesis of small-sized and highly ordered Pt-IMCs catalysts with commercial carbon black supports. The molecular additives containing coordinating heteroatoms (that is, O, N, or S) can greatly suppress the metal particle sintering in high-temperature H₂-annealing synthesis, by which the alloy nanoparticles evolve into intermetallic phases but do not suffer from severe sintering, guaranteeing the formation of small-sized IMCs nanoparticle catalysts with high ordering degree. With the optimal sodium thioglycolate additive, we demonstrate the

combinatorial synthesis of catalyst libraries consisting of 18 binary Pt-IMCs. We understand that small molecule additives are coordinated with platinum in impregnation and thermally converted into heteroatom-doped carbon shells around alloy particles, which significantly suppress particle sintering in high-temperature annealing. The prepared PtCo intermetallic catalysts exhibit a high mass activity (MA) of 1.08 A mg_{Pt}⁻¹ at 0.9 V_{iR-correct} in H₂-O₂ fuel cells and a large rated power density of 1.17 W cm⁻² at 94 °C in H₂-air fuel cells, along with an outstanding durability (MA and rated power density remained 75% and 88%, respectively, after 30,000 cycles' accelerated durability tests (ADT)).

Results

Screening molecule additives

We first screened a diversity of small molecule additives containing coordinating heteroatoms (that is, O, N, or S) for suppressing metal sintering in high-temperature H₂-annealing (Fig. 1a), by taking PtCo as examples. Molecule additives and metal precursors (i.e. H₂PtCl₆ and CoCl₂) were wet-impregnated onto carbon black supports (Ketjenblack EC-300J with a specific surface area of ~800 m² g⁻¹) with a total metal loading of 30 wt%. The powder precursors underwent annealing treatments in 5 vol% H₂/Ar at 700 °C for 4 h. The average particle size of the obtained PtCo catalysts was analyzed by the Debye–Scherer equation based on the full width at half maximum of X-ray powder diffraction (XRD) patterns and the statistical results from high-angle annular dark-field scanning transmission electron microscopy (HAADF-STEM) images (Fig. 1b and Supplementary Table 1).

We found severe PtCo sintering (XRD size of 14.9 nm) on carbon black supports in the high-temperature H₂-annealing if no molecule additives were used, which is consistent with reported

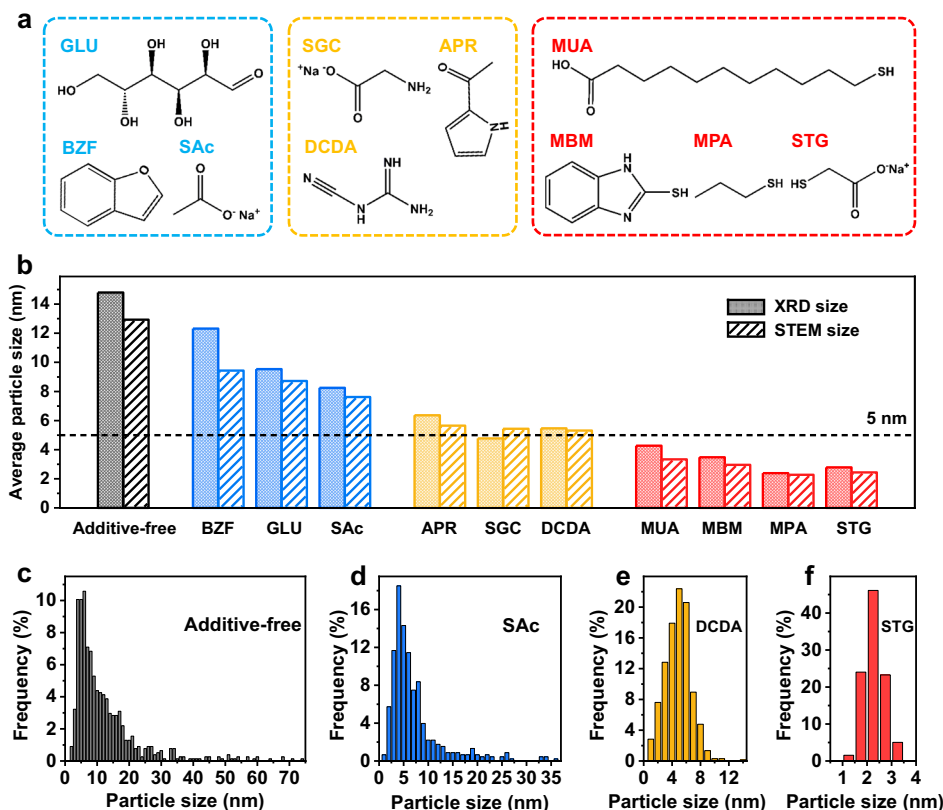


Fig. 1 | Screening small molecules for suppressing metal sintering. **a** The structures of the molecules used as additives for suppressing metal sintering. **b** XRD (solid shadow column) and STEM (twill stripes column) sizes of PtCo

particles with various molecule additives used for the catalyst synthesis at 700 °C. STEM statistics of particle size distribution of PtCo synthesized without (c) and with three representative molecule additives, including SAc (d), DCDA (e), and STG (f).

results of high-loading PtCo IMCs catalyst synthesis^{5,6}. When oxygen-containing molecule additives including glucose (GLU), sodium acetate (SAC), or 2,3-benzofuran (BZF) were used for the impregnation synthesis, the XRD size of PtCo was reduced slightly to 8–12 nm. In the cases of nitrogen-containing molecule additives such as 2-acetylpyrrole (APR), sodium glycinate (SGC), and dicyandiamide (DCDA), the XRD size of PtCo was restricted in the range of 5.5–6.5 nm. Notably, sulfhydryl group-containing molecules including 11-mercaptoundecanoic acid (MUA), 2-mercaptobenzimidazole (MBM), 1-mercaptopropane (MPA), and sodium thioglycolate (STG) exhibited outstanding capacity for suppressing PtCo sintering. Especially, the XRD average particle sizes of PtCo were only ~2.5 nm with MPA and STG used as additives in the high-temperature synthesis.

The average particle sizes obtained from the statistics of HAADF-STEM images matched well with the XRD results (Supplementary Fig. 1). We observed a very wide particle size distribution ranging from a few to tens nanometers in the additive-free synthesis; the appearance of abnormally large particles reflected the severe sintering occurred through coalescence and Ostwald ripening^{19,38,39}, which was exacerbated for the high-loading catalysts with short inter-particle distance^{40,41}. The size distribution was significantly narrowed when using molecule additives; and remarkably, no PtCo particles of >5 nm were found when using MPA or STG as additive (Fig. 1c–f and Supplementary Fig. 2).

Synthesis of Pt-IMCs catalyst libraries

Considering the anti-sintering capacity and convenience, we chose water-soluble STG as the optimal additive for the synthesis of Pt-IMCs catalyst libraries. We synthesized the Pt-IMCs catalysts by subjecting the carbon black Ketjenblack EC-300J impregnated with metal salt precursors and STG (Pt content of 20–27.7 wt%; n_{STG}/n_{Pt} of 1.5) to the high-temperature H₂-annealing treatment at 600–1000 °C. To improve the ordering degree, two-step H₂-annealing protocol was adopted for some Pt-IMCs synthesis⁶. The high-temperature-annealing step was to alloy Pt with enough amount of base metals to approach the stoichiometric ratio of corresponding Pt-IMCs structures and thus to maximize the thermodynamic driving force of disorder-to-order transition; the relatively-low-temperature-annealing step with prolonged time was to make the kinetically controlled atom ordering thoroughly proceed. For each Pt-IMCs synthesis, the temperature of high-temperature-annealing step was optimized to balance the trade-off relations between particle size and ordering degree (Supplementary Table 2). The details of the optimal synthesis recipe for each Pt-IMCs catalyst were summarized in Supplementary Table 3.

We totally synthesized 18 binary Pt-IMCs catalysts by the STG-assisted impregnation method, including Pt alloyed with 3*d* early transition metals (Pt₃Ti, Pt₃V, and Pt₃Cr), 3*d* late transition metals (Pt₃Mn, PtMn, Pt₃Fe, PtFe, Pt₃Co, PtCo, PtNi, PtCu, PtCu₃, and PtZn), group IIIA metals (Pt₃Al, Pt₃Ga, and Pt₃In), and group IVA metals (Pt₃Ge and Pt₃Sn) (Fig. 2a). The Pt-IMCs structures were evidenced by the

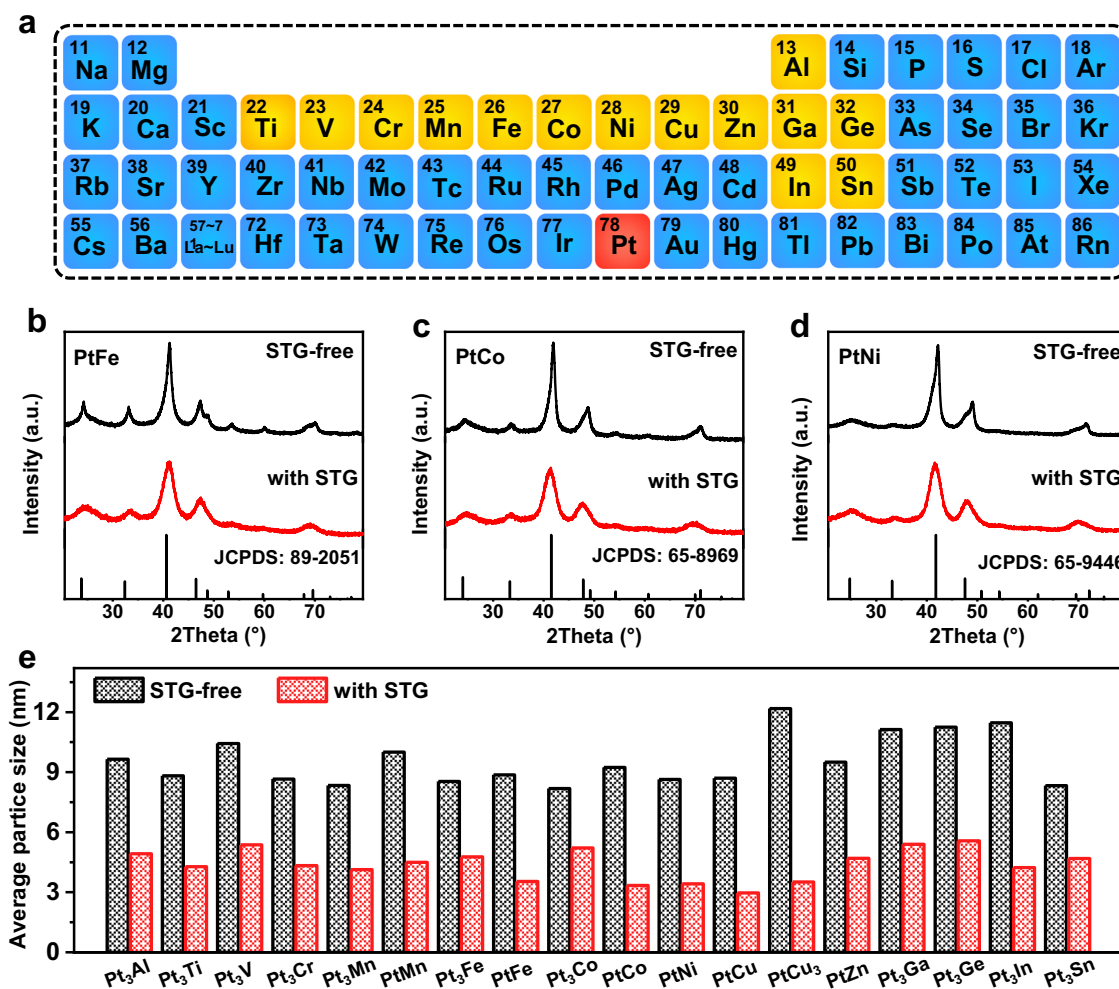


Fig. 2 | STG-assisted synthesis of Pt-IMCs catalyst libraries. **a** Periodic table showing Pt (highlighted in red) and base metal elements (highlighted in yellow) that constitute Pt-IMCs catalyst libraries. Comparison of the XRD patterns of PtFe (**b**),

PtCo (**c**), and PtNi (**d**) prepared with and without STG. **e** Comparison of XRD particle size of the 18 Pt-IMCs catalysts prepared with and without STG.

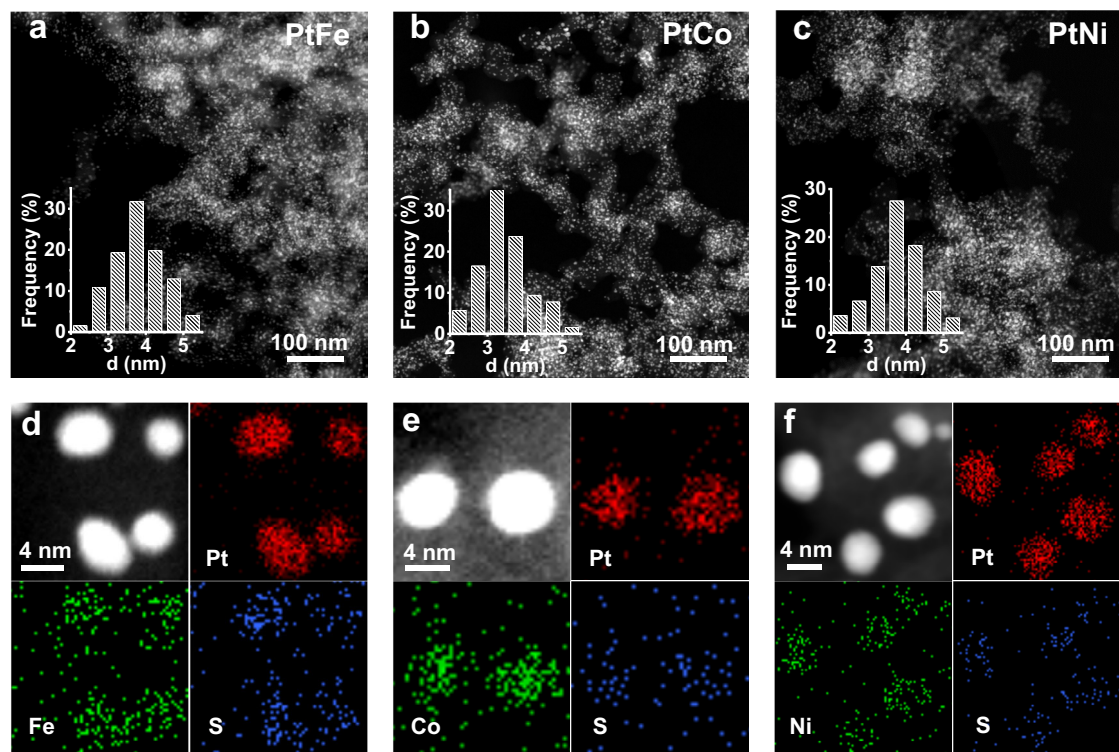


Fig. 3 | Structural characterization of the Pt-IMCs catalysts. HAADF-STEM images of PtFe (a), PtCo (b), and PtNi (c) prepared with STG. Inserts were the corresponding statistics of particle size distribution. EDS elemental mapping of PtFe (d), PtCo (e), and PtNi (f) prepared with STG.

experimental XRD patterns that showed ordering crystal structure with characteristic superlattice reflection and matched well with the corresponding Joint Committee on Powder Diffraction Standards (JCPDS) cards (Fig. 2b–d and Supplementary Fig. 3). All the Pt₃M- and PtM₃-type Pt-IMCs adopted a cubic structure in space group Pm-3m, except for Pt₃Ge whose space group was I4/mcm; all the PtM-type IMCs adopted a tetragonal structure in space group P4/mmm, except for PtCu whose space group was R-3m. The XRD average particle size of most samples (14 cases) was less than 5 nm, with four cases showing slightly large particle size (5.2–5.6 nm for Pt₃V, Pt₃Co, Pt₃Ga, and Pt₃Ge) (Fig. 2e and Supplementary Table 2). Contrastively, the XRD size of Pt-IMCs synthesized by the conventional impregnation synthesis (that is, molecule additive-free) was in the range of 8.2–12.2 nm (Fig. 2e).

HAADF-STEM observations confirmed the uniform distribution of the small-sized PtFe, PtCo, and PtNi IMCs nanoparticles on the whole carbon black supports with narrow particle size distributions (Fig. 3a–c). The statistical analyses of particle size based on the HAADF-STEM images were consistent well with the XRD results. Moreover, elemental mapping with energy-dispersive X-ray spectroscopy (EDS) showed that Pt and base metal elements were distributed uniformly in individual particles, and the atomic ratio of Pt/base metal was approximately equivalent to the corresponding stoichiometric value (Fig. 3d–f, Supplementary Figs. 4–8 and Supplementary Table 4).

We used atomic number (Z)-contrast HAADF-STEM imaging to analyze the ordered structures of three representative samples of PtCo, Pt₃Co, and PtCu on an atomic scale. For PtCo (Fig. 4a), the HAADF-STEM image along [100] direction showed the alternating arrangement of Pt and Co atom columns, represented by the brighter dots and darker dots respectively (Pt columns have a higher intensity than Co columns with a lower Z), indicating the L₁o-type face-centered tetragonal (*ftc*) intermetallic structure. For Pt₃Co (Fig. 4b), we observed periodic square array of Co columns surrounded by Pt columns at the edges and corners of each unit cell along the [001] zone axis, corresponding to the L₁2-type face-centered cubic (*fcc*)

intermetallic structure. In the case of PtCu (Fig. 4c), the alternating Pt and Cu columns were staggered to align along the [110] direction, which were assigned to the L₁1-type rhombohedral intermetallic structure. Fast Fourier transform (FFT) patterns (Supplementary Fig. 9) and alternating intensity profiles (Fig. 4) further confirmed the ordered structure of these Pt-IMCs.

The convenience and scalability of the small molecule-assisted impregnation method enabled the grams scale synthesis. We achieved the one-batch synthesis of L₁o PtCo catalyst exceeding 6 grams, with a considerable high ordering degree of 65%, a small XRD size of 4.3 nm as well as a narrow particle size distribution revealed by HAADF-STEM observations (Supplementary Fig. 10 and Supplementary Table 5). We also achieved the L₁o PtCo catalyst synthesis with a high total metal loading of 45 wt% (Pt content of 34.5 wt%), showing an ordering degree of 56% and a XRD size of 4.7 nm (Supplementary Fig. 11 and Supplementary Table 5).

Mechanism study

We performed UV-visible absorption (UV-Vis) spectroscopy, X-ray photoelectron spectroscopy (XPS), thermogravimetry-mass spectrometry (TG-MS), extended X-ray absorption fine structure (EXAFS), HAADF-STEM, and EDS elemental mapping characterizations to understand the anti-sintering mechanism of the small molecule additives, by taking STG-assisted impregnation synthesis of PtCo IMCs as a typical example. We found the discoloration from light yellow to orange when STG was added into the aqueous solution of H₂PtCl₆ (Supplementary Fig. 12), indicating the change of coordination structure of platinum. H₂PtCl₆ solution showed typical four absorption bands in its UV-Vis spectrum located at around 205, 260, 373, and 450 nm, respectively (Fig. 5a). The absorption bands at 205 and 260 nm were assigned to the ligand-to-metal charge-transfer corresponding to ¹A_{1g} → ¹T_{1u} transition; the former was due to the transitions from orbitals with ligand σ-character, while the latter was due to the transitions involving orbitals with Cl ligand π-character⁴². The

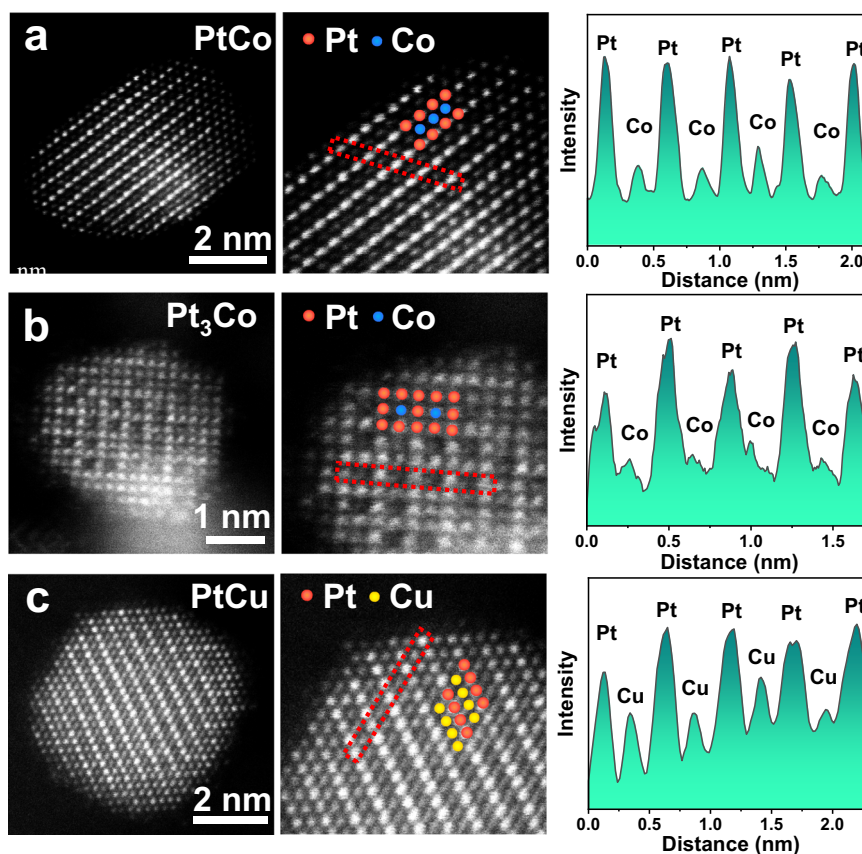


Fig. 4 | Atomic scale HAADF-STEM characterization of Pt-IMCs. Atomic-resolution HAADF-STEM images and alternative intensity profiles of PtCo (a), Pt₃Co

(b), and PtCu (c). The alternative intensity profiles were obtained from the corresponding region marked by red dashed rectangle.

absorption bands at 373 and 450 nm were assigned to the *d-d* transitions that reflected the octahedral symmetry of [PtCl₆]²⁻ configuration^{43,44}. We observed significant changes of the intensity of absorption bands at 205, 373, and 450 nm when STG was mixed with H₂PtCl₆, whereas no obvious changes of H₂PtCl₆ absorption bands were found if replacing STG with SAC that had only carboxyl group. These results suggested that the sulfhydryl group in STG coordinated with platinum by ligand exchanging with Cl⁴⁵.

In high-resolution Pt 4f XPS spectra for the H₂PtCl₆-CoCl₂/C, we assigned the peak pair located at 75/78.2 eV and peak pair located at 72.7/76 eV to the Pt (IV) and Pt (II) species, respectively⁴⁶. With the incorporation of STG molecules, we found increased content of Pt (II) species and negative shift of binding energy for Pt (IV) species by -0.3 eV in STG-H₂PtCl₆-CoCl₂/C, indicating a more electron-enriched state after ligand exchange (Fig. 5b). Differently, the binding energy of Co 2p showed a positive shift by -1.4 eV with the incorporation of STG (Fig. 5c). We supposed that the electronic structure change of Co was associated to the coordination of Co (II) with carboxylate group in STG.

TG-MS coupling technique was employed to analyze the thermal decomposition of STG in high-temperature H₂-annealing. We observed continuous weight loss of STG-H₂PtCl₆-CoCl₂/C during the whole heating process up to 900 °C (Fig. 5d). The collected signal of the characteristic fragment corresponding to CH₂-SH with the mass-to-charge ratio of 47 appeared at 257 °C and 566 °C, while only one single peak of CH₂-SH signal at a lower temperature of -254 °C was found for STG/C (Fig. 5e). Thus, the decomposition peak at the high temperature of 566 °C could be assigned to STG coordinated to platinum. Fourier-transformed EXAFS analyses showed a clear trend that the intensity of Pt-Cl/Pt-S bonds gradually decreased as the annealing temperature rising, accompanied by the increased intensity of Pt-Pt/Pt-Co bonds

(Supplementary Fig. 13), demonstrating the decomposition of coordination structures and the formation of alloys.

After high-temperature H₂-annealing of the STG-H₂PtCl₆-CoCl₂/C composite precursor, we observed by high-resolution bright-field STEM that a one-graphene-layer carbon coating with lower contrast almost completely covered the alloy particles and connected with the underlying carbon support (Supplementary Fig. 14). EDS elemental mapping revealed that the majority of residual S elements concentrated on the PtCo particle region (Fig. 3e). Note that the S/Pt atomic ratio has dramatically decreased from 1.5 for the precursor to 0.15 after the annealing (Supplementary Fig. 5). Considering the spatial relationship between S, carbon shells and PtCo particles, we could reasonably infer that S atoms were doped in the carbon layers on the PtCo particle surface. In the Fourier-transformed EXAFS (Fig. 5f), the annealed sample showed an extra shoulder peak similar as the Pt-S bond in PtS₂, indicating the binding interaction between Pt and doped S atoms in carbon shells. We also characterized several additional STG-assisted Pt intermetallic catalysts including PtFe, PtNi, Pt₃Ti, and Pt₃In by high-resolution STEM (Supplementary Fig. 15), the results showed that the carbon shell formation was a general phenomenon in the STG-assisted synthesis.

On the basis of the above systematical characterizations, we propose the anti-sintering mechanism in the STG-assisted synthesis of PtCo IMCs (Fig. 5g). In the initial wet-impregnation step, the sulfhydryl group of STG tended to coordinate with Pt (IV) via the partial ligand exchange with Cl, meanwhile the carboxylate group in STG coordinated with Co (II), to form bimetallic complex network (left panel in Fig. 5g). Upon the annealing, the complex precursors gradually decomposed, along with the release of CH₂-SH and Cl fragments and the formation of the PtCo bimetallic clusters. The coordinated STG ligands exhibited promoted thermal stability compared to

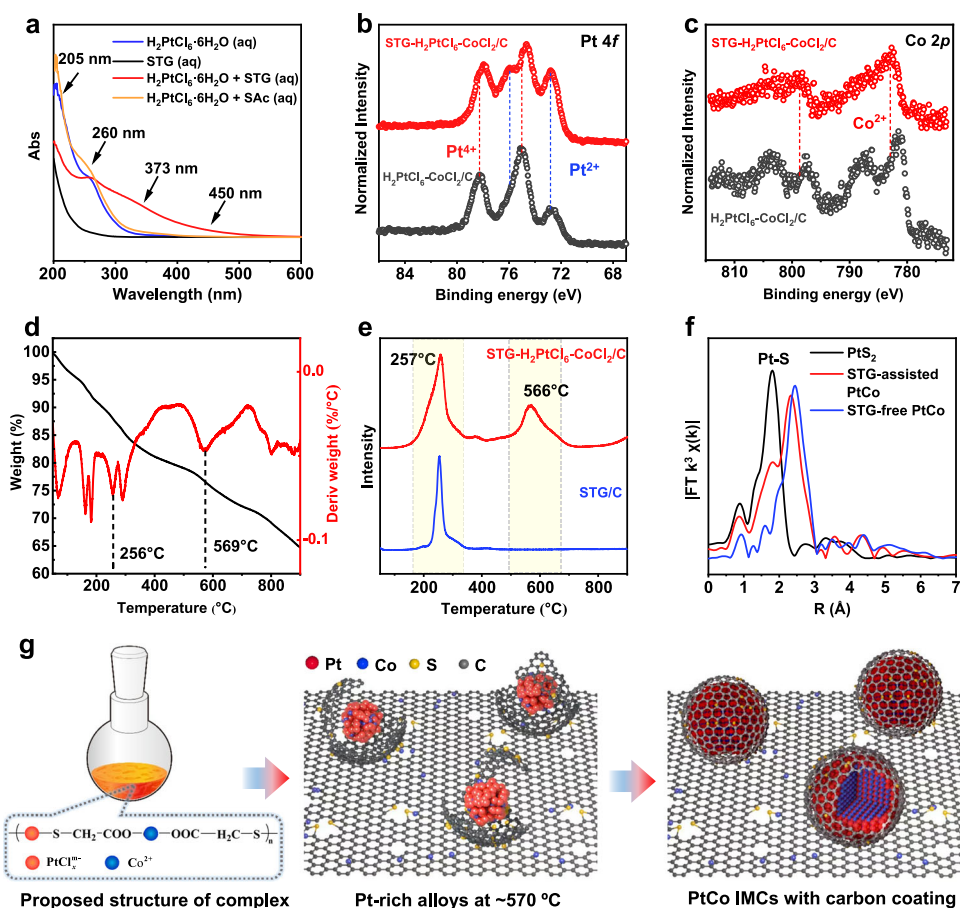


Fig. 5 | Anti-sintering mechanism. **a** UV-Vis spectra of the $\text{H}_2\text{PtCl}_6 \cdot 6\text{H}_2\text{O}$ solution, STG solution, the $\text{H}_2\text{PtCl}_6 \cdot 6\text{H}_2\text{O}$ /STG solution, and the $\text{H}_2\text{PtCl}_6 \cdot 6\text{H}_2\text{O}$ /SAC solution. XPS results of the Pt 4f (**b**) and Co 2p (**c**) orbitals of the STG-PtCo/C precursor powder and PtCo/C precursor powder. **d** TG result of STG-PtCo/C raw powder

from room temperature to 900 °C. **e** MS signal of $\text{CH}_2\text{-SH}$ fragment obtained from the STG/C powder and STG-PtCo/C precursor powder. **f** R space of the XAFS results of the standard PtS_2 , and PtCo IMCs catalysts prepared with and without STG. **g** Proposed anti-sintering mechanism of the STG-assisted method.

uncoordinated STG as revealed by the TG-MS tests and thus thermally converted to S-doped carbonaceous layers around the PtCo clusters (middle panel in Fig. 5g). Further annealing at the evaluated temperature of 900 °C made the PtCo particles well alloyed with targeted stoichiometric ratio (that is 1:1 for Ll_0 PtCo IMCs). In the final low-temperature-annealing step with prolonged time (600 °C, 6 h), the Pt/Co atoms rearranged into intermetallic structures via a kinetically controlled atom ordering process. Importantly, the physical protective carbon coating and the chemical Pt-S interaction, may function in a synergetic way, to greatly suppress the PtCo sintering during the high-temperature annealing and guaranteed the synthesis of small-sized Pt-IMCs catalysts (right panel in Fig. 5g). The detailed anti-sintering mechanism should differ with various molecule additives, as the capacity for suppressing PtCo sintering was strongly dependent on the molecule structures. But our results demonstrated the general validity of utilizing small molecule additives for the impregnation synthesis of small-sized Pt-IMCs catalysts.

PEMFCs performance

Six PtM-type IMCs catalysts were selected for the electrochemical measurements, including five Ll_0 structures (PtMn, PtFe, PtCo, PtNi, and PtZn) and one Ll_1 structure (PtCu). Prior to tests, all the catalysts were first oxidized in air (230 °C, 6 h) to gently remove the carbon coating and exposure metal surface evidenced by the STEM images of the samples after air oxidation (Supplementary Fig. 16). EDS mapping demonstrated that the S/Pt atomic ratio was reduced to 0.016 after the oxidation treatment, corresponding to a nearly 10 times of reduction

relative to the value of pristine catalyst (0.15). Then the powder underwent acid leaching (0.2 M H_2SO_4 , 60 °C, 12 h) and low-temperature H_2 -annealing (5 vol% H_2/Ar , 400 °C, 2 h) treatments successively to form an electrochemically stable and active core/shell structures that were composed of an intermetallic PtCo core and two to three atomic layers of Pt shell (Supplementary Fig. 17)^{6,47–49}.

In the rotating disk electrode (RDE) tests, all the six catalysts showed high electrochemically active surface areas (ECSA) of 63.4–86.7 $\text{m}^2 \text{g}_{\text{Pt}}^{-1}$ tested by CO-stripping, which is comparable with that of commercial TKK-30 wt% Pt/C (72.5 $\text{m}^2 \text{g}_{\text{Pt}}^{-1}$) and higher than that of recently reported PtM IMCs catalysts^{13,14,35,50}. The PtM IMCs catalysts also showed much higher mass activities of 0.88–2.25 $\text{A mg}_{\text{Pt}}^{-1}$ and specific activities of 1.12–3.33 mA cm^{-2} at 0.9 $V_{\text{IR-correct}}$ than those of Pt/C (0.35 $\text{A mg}_{\text{Pt}}^{-1}$ for MA; 0.48 mA cm^{-2} for specific activity) (Fig. 6a, b and Supplementary Table 6). We further observed a strong relationship between ORR activity and surface compressive strain for all the five Ll_0 IMCs catalysts (Fig. 6c and Supplementary Table 7), consistent with our previous results on S-doped carbon supported IMCs catalysts⁶. We predict that further promotion of ORR activity would be realized by shortening the lattice parameter of the intermetallic core to enhance the surface compressive strain.

Finally we chose the STG-assisted PtCo as the cathode catalyst for the PEMFCs tests. The TKK-30 wt% Pt/C, TKK-30 wt% Pt/C annealed at 700 °C for 2 h (named as TKK-30 wt% Pt/C-700), and the Elyst Pt30 0690 catalysts from Umicore (named as Umic-30 wt% PtCo) were also tested as the comparison. The ionomer to carbon (I/C) ratio was optimized for each cathode catalysts (Supplementary Fig. 18). In $\text{H}_2\text{-O}_2$

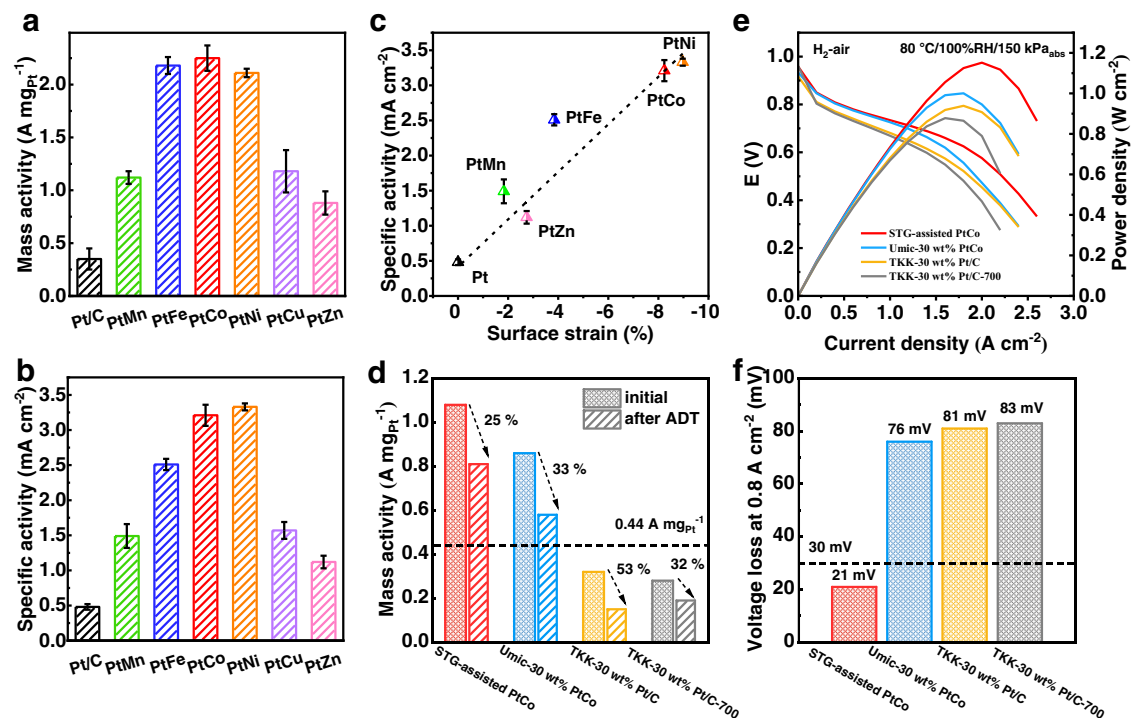


Fig. 6 | Electrocatalytic performance. RDE mass activity (a), and specific activity (b) of the STG-assisted Pt-IMCs catalysts and TKK-30 wt% Pt/C. The Pt loading in RDE tests were in the range of 11–13 $\mu\text{g cm}^{-2}$. c Correlation between specific activity and calculated surface strain of the five L10 PtM catalysts and Pt/C. The error bars in a, b, and c were obtained after three parallel experiments. d Mass activity loss of the MEAs made with cathode catalysts of STG-assisted PtCo, Umic-30 wt% PtCo, TKK-30 wt% Pt/C, and TKK-30 wt% Pt/C-700 after 30,000 cycles' ADT. e H_2 -air polarization curves and power density plots of the MEAs made with cathode catalysts of

STG-assisted PtCo, Umic-30 wt% PtCo, TKK-30 wt% Pt/C, and TKK-30 wt% Pt/C-700. For all MEA, the cathode and anode loadings were controlled to be 0.1 and 0.025 $\text{mg}_{\text{Pt}} \text{cm}^{-2}$, respectively. Test conditions: 80 °C, 100% RH, 150 kPa_{abs} , outlet H_2 -air at high stoichiometries (H_2 and air flow rates were fixed at 0.5 and 2.0 L min^{-1} , respectively). f Voltage loss at 0.8 A cm^{-2} of the MEAs made with cathode catalysts of STG-assisted PtCo, Umic-30 wt% PtCo, TKK-30 wt% Pt/C, and TKK-30 wt% Pt/C-700 after 30,000 cycles' ADT.

single-cell test, STG-assisted PtCo catalyst exhibited a high MA of 1.08 $\text{A mg}_{\text{Pt}}^{-1}$ at 0.9 V, higher than 0.32, 0.28, and 0.86 $\text{A mg}_{\text{Pt}}^{-1}$ for TKK-30 wt% Pt/C, TKK-30 wt% Pt/C-700, and Umic-30 wt% PtCo, respectively, and exceeded the US Department of Energy (DOE) 2025 target of 0.44 $\text{A mg}_{\text{Pt}}^{-1}$. After 30,000 cycles' ADT, which was performed by a square wave voltage cycling from 0.6 to 0.95 V with a duration of 3 s for each voltage, the MA of the STG-assisted PtCo catalyst declined by 25%, while for TKK-30 wt% Pt/C, TKK-30 wt% Pt/C-700, and Umic-30 wt% PtCo, the MA declined by 53%, 32%, and 33%, respectively (Fig. 6d).

We further tested the performance of STG-assisted PtCo catalyst in H_2 -air single cell. At the test conditions of 80 °C, 100% relative humidity (RH), and 150 kPa_{abs} , the current density at 0.8 V for the cathode made of the STG-assisted PtCo catalyst was 412 mA cm^{-2} , slightly higher than that of Umic-30 wt% PtCo cathode (395 mA cm^{-2}), much higher than that of TKK-30 wt% Pt/C (250 mA cm^{-2}) and TKK-30 wt% Pt/C-700 (216 mA cm^{-2}), and exceeded the DOE 2025 target of 300 mA cm^{-2} (Fig. 6e and Supplementary Table 8). After 30,000 cycles' ADT, the voltage loss of the STG-assisted PtCo cathode at 0.8 A cm^{-2} was 21 mV, well meeting the DOE 2025 target (less than 30 mV loss); while for TKK-30 wt% Pt/C, TKK-30 wt% Pt/C-700, and Umic-30 wt% PtCo cathodes, the voltage loss was 83, 81, and 76 mV, respectively (Fig. 6f and Supplementary Fig. 19). H_2 -air single-cell tests were also performed at 94 °C, 65% RH, and 250 kPa_{abs} , considering the US DOE target of $Q/\Delta T < 1.45 \text{ kW } ^\circ\text{C}^{-1}$ for heat rejection^{51,52}. The rated power density of the STG-assisted PtCo cathode at 94 °C reached 1.17 W cm^{-2} , much higher than that of TKK-30 wt% Pt/C (0.79 W cm^{-2}), TKK-30 wt% Pt/C-700 (0.73 W cm^{-2}), and Umic-30 wt% PtCo (0.94 W cm^{-2}) cathodes. After 30,000 cycles' ADT, the rated power density of the STG-assisted PtCo cathode still reached 1.03 W cm^{-2} (Supplementary Fig. 19).

Discussion

In summary, we developed a small molecule-assisted impregnation method for the general synthesis of small-sized Pt-IMCs in grams scale with commercial carbon black supports. The molecular additives containing functional groups (particularly sulfhydryl) acted as ligands to coordinate with Pt (IV) in impregnation and then thermally converted into heteroatom-doped graphene layers coating on alloy nanoparticles, which greatly suppressed metal sintering in high-temperature annealing and guaranteed the formation of small-sized Pt-IMCs catalysts. By the molecule-assisted approach, we demonstrated the combinatorial synthesis of intermetallic catalyst libraries consisting of 18 binary Pt-IMCs. The intermetallic libraries were highly mass efficient as low-Pt cathode catalysts in PEMFCs with a high mass activity of 1.08 $\text{A mg}_{\text{Pt}}^{-1}$ and could achieve a high rated power density of 1.17 W cm^{-2} . Although we demonstrated the PEMFCs applications in the current work, the Pt intermetallics catalysts library has also great application potentials for other energy-conversion-related electrocatalysis and heterogeneous catalysis, for example, electrocatalytic oxidation²⁹, alkane dehydrogenation⁵³, and acetylene semi-hydrogenation⁵⁴. Moreover, the combinatorial synthesis of the intermetallic catalysts spanning a wide range of metal elements would allow a comprehensive exploration of a structure-performance relationship for diverse reactions in a systematic manner.

Methods

Screening small molecules for suppressing metal sintering

A diversity of small molecules containing coordinating heteroatoms (Fig. 1a) as additives were screened for suppressing metal sintering by

taking PtCo for an example in the wet-impregnation synthesis. 0.168 mmol $\text{H}_2\text{PtCl}_6 \cdot 6\text{H}_2\text{O}$ and 0.252 mmol molecule were first dissolved in 30 mL solvent (deionized water for GLU, SAc, APR, SGC, DCDA, and STG; acetone for BZF, MUA, and MBM; hexane for MPA) by stirring in a 100 mL flask for 10 min. Then, 0.218 mmol $\text{CoCl}_2 \cdot 6\text{H}_2\text{O}$ was added and stirred for another 10 min to form a clear mixed solution. 100 mg carbon black (Ketjenblack EC-300J) was added into the above solution and stirred overnight to form a homogeneous dispersion, which was then dried with a rotary evaporator. Finally, the raw powder was annealed at 700 °C for 4 h, followed with naturally cooling down to room temperature. The obtained sample were washed thoroughly by deionized water and then underwent XRD and microscopic characterization to elevate the anti-sintering capacitor of the molecule additives.

STG-assisted synthesis of Pt-IMCs catalyst libraries

The precursors containing carbon black supports, $\text{H}_2\text{PtCl}_6 \cdot 6\text{H}_2\text{O}$ and base metal salts, as well as the optimal molecule additive (that is, STG) were prepared by the same wet-impregnation procedure described above. The obtained precursors were then subjected to one- or two-step high-temperature H_2 -annealing treatment at 600 to 1000 °C to form Pt-IMCs. For each sample, the annealing temperature was optimized to balance the trade-off between particle size and ordering degree. The data of the optimizing process of the PtCo synthesis was shown in Supplementary Fig. 20 and Supplementary Table 5. Typically, for the optimal synthesis of PtCo IMCs, the precursors composed of 100 mg carbon black, 87 mg $\text{H}_2\text{PtCl}_6 \cdot 6\text{H}_2\text{O}$ (0.168 mmol), 51.9 mg $\text{CoCl}_2 \cdot 6\text{H}_2\text{O}$ (0.218 mmol), and 29 mg STG (0.252 mmol) underwent two-step high-temperature H_2 -annealing treatment (900 °C for 2 h and 600 °C for 6 h in sequence) with a heating/cooling rate of 10 °C min^{-1} . The obtained sample were finally washed thoroughly by deionized water. The optimal synthesis recipes for each Pt-IMC catalyst were summarized in Supplementary Table 3. For comparison, Pt-IMCs were also synthesized without molecule additives by the same procedure.

For the grams scale synthesis, the whole synthesis procedure was identical as above, except for expanding the dosage to 8.4 mmol $\text{H}_2\text{PtCl}_6 \cdot 6\text{H}_2\text{O}$, 12.6 mmol STG, 10.9 mmol $\text{CoCl}_2 \cdot 6\text{H}_2\text{O}$, 5 g carbon black, and 800 mL deionized water in the wet-impregnation step.

For the synthesis of high-loading PtCo IMCs, the precursors composed of 100 mg carbon black, 166.7 mg $\text{H}_2\text{PtCl}_6 \cdot 6\text{H}_2\text{O}$ (0.322 mmol), 99.5 mg $\text{CoCl}_2 \cdot 6\text{H}_2\text{O}$ (0.418 mmol), and 55.5 mg STG (0.483 mmol) underwent two-step high-temperature H_2 -annealing treatment (750 °C for 2 h and 600 °C for 4 h in sequence) before being washed thoroughly by deionized water. The nominal total metal content was 45 wt% and the nominal Pt content was 34.5 wt%.

Calculation of the ordering degree

To calculate the ordering degree of different Pt-IMCs samples, we used the ratio of the intensity or integrated area of superlattice reflection to non-characteristic reflections as a quantitative evaluation¹⁹. For example, for PtCo, we used the ratio of integrated area under (110) plane to the sum of the areas under (111), (200) and (002) planes, $S_{(110)}/(S_{(111)} + S_{(200)} + S_{(002)})$, as a quantitative evaluation. The value of $S_{(110)}/(S_{(111)} + S_{(200)} + S_{(002)})$ for the standard *fcc*-PtCo (JCPDS: 65-8969) is 0.1677, which corresponds to 100% ordering intermetallic PtCo, then the ratio of $S_{(110)}/(S_{(111)} + S_{(200)} + S_{(002)})$ calculated from PtCo prepared with STG to 0.1677 is the corresponding ordering degree.

Calculation of the surface strain of Ll_0 PtM catalysts

The surface strain was calculated based on the area change of intermetallic structure relative to bulk Pt. The areas of the triangles shown in Supplementary Fig. 21 can be calculated by the Heron's formula as

follows:

$$p = 1/2(l_{(110)} + l_{(101)} + l_{(011)}) \quad (2)$$

$$S = \sqrt{p(p - l_{(110)})(p - l_{(101)})(p - l_{(011)})} \quad (3)$$

$$\text{Surface strain} = \frac{S_{\text{IMC}} - S_{\text{bulkPt}}}{S_{\text{bulkPt}}} \times 100\% \quad (4)$$

where $l_{(110)}$, $l_{(101)}$, and $l_{(011)}$ represent the length of three triangle sides ($l = 2 \times d_{\text{Pt-Pt}}$ or $d_{\text{Pt-M}}$). The calculated surface strain for all the *fcc* intermetallic catalysts was summarized in Supplementary Table 7.

Characterization

XRD patterns were obtained on a Japan Rigaku DMax- γ A rotating anode X-ray diffractometer using Cu K- α radiation ($\lambda = 1.54056 \text{ \AA}$) at 40 kV and 150 mA. UV-Vis spectra were measured on a UV-3600i plus spectrometer. XPS measurement was carried out on an X-ray photoelectron spectrometer (ESCALab MKII) with an excitation source of Mg K α radiation (1253.6 eV). TG-MS were measured with TGA-8000 thermogravimetry and Clarus SQ 8Tmass spectrometer. Atomic-resolution HAADF-STEM images and high-resolution bright-field STEM images were taken by a JEM-ARM 200 F Atomic Resolution Analytical Microscope operating at 200 kV. Low-magnification HAADF-STEM images and EDS mapping images were obtained on FEI Talos F200X, equipped with Super X-EDS system at 200 kV. Inductively coupled plasma atomic emission spectrometry (ICP-AES) measurements were carried out on a Thermo Scientific iCAP 7400. X-ray absorption spectra were measured at the beamline 1WIB station of the Beijing Synchrotron Radiation Facility (BSRF) operated at 2.5 GeV and 250 mA.

RDE measurements

Five Ll_0 catalysts (PtMn, PtFe, PtCo, PtNi, and PtZn) and one Ll_1 catalyst (PtCu) were selected for the electrocatalytic studies. Prior to electrocatalytic tests, all the catalysts were treated successively by air oxidation (230 °C, 6 h), acid leaching (0.2 M H_2SO_4 , 60 °C, 12 h), and low-temperature H_2 -annealing (5 vol.% H_2/Ar , 400 °C, 2 h) to remove carbon coating and to form active and stable Pt-IMCs@Pt core/shell structures. The nominal total metal loading of the pristine catalysts was 30 wt%. The exact Pt contents of the treated catalysts used for electrochemical measurements were quantified by ICP-AES to be 25.7 wt% for PtMn, 24.6 wt% for PtFe, 24.5 wt% for PtCo, 23.5 wt% for PtNi, 24.3 wt% for PtCu, and 22.1 wt% for PtZn.

RDE measurements were performed by using a CHI Electrochemical Station (Model 760E) in a three-electrode electrochemical cell at room temperature. Hg/Hg $_2$ SO $_4$ was used as a reference electrode and Pt foil was used as a counter electrode. The reference electrode potentials in this work were calibrated to the reversible hydrogen electrode (RHE) potentials under hydrogen-saturated 0.1 M HClO $_4$ solution for each test. The catalyst ink was prepared by sonicating the mixture consisting of 4 mg catalyst and 40 μL (5 wt%) Nafion in 2 mL isopropanol. Then, the ink was drop-coated onto the working electrode (a glassy carbon disk with diameter 5.0 mm) with Pt loading of 11–13 $\mu\text{g cm}^{-2}$ and dried at room temperature in air. After drying, the catalysts were electrochemically activated by cyclic voltammetry (CV) scanning between 0.05 and 1.05 V at 250 mV s^{-1} in N_2 -saturated 0.1 M HClO $_4$ solution (around 200 cycles). Then the linear scanning voltammetry (LSV) curves were obtained from 0.05 V to 1.05 V at 10 mV s^{-1} in O_2 -saturated 0.1 M HClO $_4$ with the rotating speed at 1600 rpm (Supplementary Fig. 22).

The mass related kinetic current density (j_k) of catalyst at 0.9 V vs. RHE was calculated according to: $j_k = j \times j_L / (j_L - j) \times L_{\text{Pt}}$, where j , j_L , and L_{Pt} represent the current density at 0.9 V vs. RHE, the diffusion limited current density and Pt loading, respectively. Capacitance-correction

and IR-correction were performed for the MA calculation on the WaveDriver 20 bipotentiostat (Pine Instrument Company, USA) in 0.1 M HClO₄ solution from 0.1 Hz to 10,000 Hz with an amplitude of 5 mV, the initial potential was set as 0.05 V.

The electrochemical active surface area (ECSA) was calculated from CO-stripping curve (Supplementary Fig. 23). CO-stripping test was conducted by first bubbling CO into 0.1 M HClO₄ electrolyte and holding potential at 0.05 V for 30 min, followed by bubbling N₂ into the electrolyte for 30 min. Then CV curve was collected by scanning from 0.05 V to 1.05 V at a scanning rate of 20 mV s⁻¹. The ECSA was calculated according to: $ECSA = (S_{CO}/V)/(0.42 \times L_{Pt})$. S_{CO} , V , and L_{Pt} represent the integration area of CO desorption, sweep speed, and Pt loading, respectively.

PEMFCs tests

The cathode catalyst ink was made by mixing the TKK-30 wt% Pt/C, TKK-30 wt% Pt/C-700, Umic-30 wt% PtCo, or treated STG-assisted PtCo catalyst with the ionomer solution (D2020® perfluorosulfonic acid ionomer with an equivalent weight of 950 g mol⁻¹) and a water-n-propanol solvent mixture (the water to n-propanol ratio was 1), followed by sonicating the dispersion in ice water for 1.5 h. The I/C ratio ranging from 0.6 to 0.9 for the four catalysts was screened to obtain the optimal performance. The optimization process showed that the MEAs made with cathode catalysts of TKK-30 wt% Pt/C, TKK-30 wt% Pt/C-700, and STG-assisted PtCo exhibited the optimal performance with the I/C ratio of 0.8, while the Umic-30 wt% PtCo cathode exhibited the optimal performance with the I/C of 0.9 (Supplementary Fig. 18). The preparation of the anode catalyst ink using TKK-30 wt% Pt/C was similar with the cathode ink except for setting the I/C ratio to 0.8. The concentrations of cathode and anode catalyst inks were all 5 mg mL⁻¹. The catalyst-coated-membrane (CCM) with an active area of 5 cm² was prepared on Nafion membrane (GORE, -12 μm) with an ultrasonic spray equipment (Siansonic UC320, Siansonic Technology Co., Ltd). The fabricated CCM was dried to completely evaporate the solvents. A gas diffusion layer (GDL) including a microporous layer was used (Freudenberg H24CX483) with a thickness of 230 μm. Two GDLs, two gaskets (140 μm), and the prepared CCM were pressed to obtain the membrane electrode assembly (MEA). The Pt loadings of all MEAs at cathode and anode were controlled to be 0.1 and 0.025 mg_{Pt} cm⁻², respectively.

The seven channel serpentine flow field was applied for the all single-cell tests. The pressure drop between the inlet and outlet of the flow field was negligible. The MEAs were tested in the Scribner 850e fuel cell test stand linked with a Scribner 885 potentiostat at 80/94 °C, 150/250 kPa_{abs} and 100/65% RH.

For the H₂-O₂ single-cell tests, the cell temperature was maintained at 80 °C. The backpressure was set at 50 kPa to compensate the steam pressure so that the net pressure of H₂ or O₂ was maintained at 100 kPa. Prior to the data collection, an activation was applied by scanning the voltage from open circuit voltage to 0.2 V, and then performing a voltage recovery (VR) process in the condition of 40 °C, 150% RH, 150 kPa_{abs} with H₂/air flow at a constant voltage of 0.2 V for 2-4 h, until a stable polarization curve was obtained⁵⁵. The MA was collected at 0.9 V_{IR-correct}, 80 °C, 100% RH, 150 kPa_{abs} H₂-O₂ at flow rates of 0.2/0.5 L min⁻¹. The fuel cell was operated at 0.9 V_{IR-correct} for 15 min and the MA was based on the average current density at the last 1 min.

For the H₂-air single-cell tests, the test conditions were 80 °C/100% RH/150 kPa_{abs} or 94 °C/65% RH/250 kPa_{abs}. H₂ and air flow rates were fixed at 0.5 and 2 L min⁻¹, respectively. The ADT test was performed using a square wave voltage from 0.6 to 0.95 V with a duration of 3 s for each voltage level, and run up to 30,000 cycles at 80 °C, atmosphere pressure, 100% RH, with H₂/N₂ flow of 0.1/0.075 L min⁻¹ for the anode and cathode, respectively.

Data availability

The additional XRD patterns, STEM images, XAFS results, catalysis performance, and ChemDraw structures data generated in this study are provided in the Supplementary Information/Source Data file.

References

1. Armbruster, M. et al. Al₁₃Fe₄ as a low-cost alternative for palladium in heterogeneous hydrogenation. *Nat. Mater.* **11**, 690–693 (2012).
2. Dasgupta, A. et al. Atomic control of active-site ensembles in ordered alloys to enhance hydrogenation selectivity. *Nat. Chem.* **14**, 523–529 (2022).
3. Furukawa, S. & Komatsu, T. Intermetallic compounds: promising inorganic materials for well-structured and electronically modified reaction environments for efficient catalysis. *ACS Catal.* **7**, 735–765 (2017).
4. Wang, X. X., Swihart, M. T. & Wu, G. Achievements, challenges and perspectives on cathode catalysts in proton exchange membrane fuel cells for transportation. *Nat. Catal.* **2**, 578–589 (2019).
5. Wang, D. L. et al. Structurally ordered intermetallic platinum-cobalt core-shell nanoparticles with enhanced activity and stability as oxygen reduction electrocatalysts. *Nat. Mater.* **12**, 81–87 (2013).
6. Yang, C.-L. et al. Sulfur-anchoring synthesis of platinum intermetallic nanoparticle catalysts for fuel cells. *Science* **374**, 459–464 (2021).
7. Antolini, E. Alloy vs. intermetallic compounds: effect of the ordering on the electrocatalytic activity for oxygen reduction and the stability of low temperature fuel cell catalysts. *Appl. Catal. B* **217**, 201–213 (2017).
8. Hodnik, N. et al. Effect of ordering of PtCu₃ nanoparticle structure on the activity and stability for the oxygen reduction reaction. *Phys. Chem. Chem. Phys.* **16**, 13610–13615 (2014).
9. Bu, L. et al. Biaxially strained PtPb/Pt core/shell nanoplate boosts oxygen reduction catalysis. *Science* **354**, 1410–1414 (2016).
10. Li, J. et al. Anisotropic strain tuning of L10 ternary nanoparticles for oxygen reduction. *J. Am. Chem. Soc.* **142**, 19209–19216 (2020).
11. Gamler, J. T. L., Ashberry, H. M., Skrabalak, S. E. & Koczkur, K. M. Random alloyed versus intermetallic nanoparticles: a comparison of electrocatalytic performance. *Adv. Mater.* **30**, e1801563 (2018).
12. Kim, H. Y. et al. Activity origin and multifunctionality of Pt-based intermetallic nanostructures for efficient electrocatalysis. *ACS Catal.* **9**, 11242–11254 (2019).
13. Li, J. R. et al. Fe stabilization by intermetallic L1(O)-FePt and Pt catalysis enhancement in L1(O)-FePt/Pt nanoparticles for efficient oxygen reduction reaction in fuel cells. *J. Am. Chem. Soc.* **140**, 2926–2932 (2018).
14. Li, J. R. et al. Hard-magnet L1(O)-CoPt nanoparticles advance fuel cell. *Catal. Joule* **3**, 124–135 (2019).
15. Yan, Y. et al. Intermetallic nanocrystals: syntheses and catalytic applications. *Adv. Mater.* **29**, 1605997 (2017).
16. Feng, Q. C. et al. Strain engineering to enhance the electrooxidation performance of atomic-layer Pt on intermetallic Pt₃Ga. *J. Am. Chem. Soc.* **140**, 2773–2776 (2018).
17. Wang, Y. F. et al. Rapid room-temperature synthesis of a metastable ordered intermetallic electrocatalyst. *J. Am. Chem. Soc.* **141**, 2342–2347 (2019).
18. Sun, D. et al. Ordered intermetallic Pd₃Bi prepared by an electrochemically induced phase transformation for oxygen reduction electrocatalysis. *ACS Nano* **13**, 10818–10825 (2019).
19. Xiong, Y. et al. Revealing the atomic ordering of binary intermetallics using in situ heating techniques at multilength scales. *Proc. Natl Acad. Sci. USA* **116**, 1974–1983 (2019).
20. Li, J. & Sun, S. Intermetallic nanoparticles: synthetic control and their enhanced electrocatalysis. *Acc. Chem. Res.* **52**, 2015–2025 (2019).

21. Cheng, H. et al. Subsize Pt-based intermetallic compound enables long-term cyclic mass activity for fuel-cell oxygen reduction. *Proc. Natl Acad. Sci. USA* **118**, e2104026118 (2021).
22. Gatalo, M. et al. A double-passivation water-based galvanic displacement method for reproducible gram-scale production of high-performance platinum-alloy electrocatalysts. *Angew. Chem. Int. Ed.* **58**, 13266–13270 (2019).
23. Luo, M., Sun, Y., Wang, L. & Guo, S. Tuning multimetallic ordered intermetallic nanocrystals for efficient energy electrocatalysis. *Adv. Energy Mater.* **7**, 1602073 (2016).
24. Kim, H. Y. et al. Intermetallic PtCu nanoframes as efficient oxygen reduction electrocatalysts. *Nano Lett.* **20**, 7413–7421 (2020).
25. Guan, J. Y. et al. Intermetallic FePt@PtBi core-shell nanoparticles for oxygen reduction electrocatalysis. *Angew. Chem. Int. Ed.* **60**, 21899–21904 (2021).
26. Yang, Z. J., Yang, H. Z., Shang, L. & Zhang, T. R. Ordered PtFeIr intermetallic nanowires prepared through a silica-protection strategy for the oxygen reduction reaction. *Angew. Chem. Int. Ed.* **61**, e202113278 (2022).
27. Chung, D. Y. et al. Highly durable and active PtFe nanocatalyst for electrochemical oxygen reduction reaction. *J. Am. Chem. Soc.* **137**, 15478–15485 (2015).
28. Du, X. X., He, Y., Wang, X. X. & Wang, J. N. Fine-grained and fully ordered intermetallic PtFe catalysts with largely enhanced catalytic activity and durability. *Energy Environ. Sci.* **9**, 2623–2632 (2016).
29. Qi, Z. et al. Sub-4 nm PtZn intermetallic nanoparticles for enhanced mass and specific activities in catalytic electrooxidation reaction. *J. Am. Chem. Soc.* **139**, 4762–4768 (2017).
30. Kim, J., Lee, Y. & Sun, S. Structurally ordered FePt nanoparticles and their enhanced catalysis for oxygen reduction reaction. *J. Am. Chem. Soc.* **132**, 4996–4997 (2010).
31. Liang, J. et al. Tungsten-doped L10-PtCo ultrasmall nanoparticles as a high-performance fuel cell cathode. *Angew. Chem. Int. Ed.* **131**, 15617–15623 (2019).
32. Chen, H. et al. A surfactant-free strategy for synthesizing, and processing intermetallic platinum-based nanoparticle catalysts. *J. Am. Chem. Soc.* **134**, 18453–18459 (2012).
33. Spendelow, J. S. *Advanced Electrocatalysts through Crystallographic Enhancement* (US DOE, 2019). https://www.energy.gov/sites/prod/files/2019/08/f65/fcto_webinarslides_spendelow_073119.pdf
34. Choi, D. S., Robertson, A. W., Warner, J. H., Kim, S. O. & Kim, H. Low-temperature chemical vapor deposition synthesis of Pt–Co alloyed nanoparticles with enhanced oxygen reduction reaction catalysis. *Adv. Mater.* **28**, 7115–7122 (2016).
35. Yoo, T. Y. et al. Direct synthesis of intermetallic platinum-alloy nanoparticles highly loaded on carbon supports for efficient electrocatalysis. *J. Am. Chem. Soc.* **142**, 14190–14200 (2020).
36. Cheng, Q. Q. et al. High-loaded sub-6 nm Pt1Co1 intermetallic compounds with highly efficient performance expression in PEMFCs. *Energy Environ. Sci.* **15**, 278–286 (2022).
37. Pavko, L. et al. Toward the continuous production of multigram quantities of highly uniform supported metallic nanoparticles and their application for synthesis of superior intermetallic Pt-Alloy ORR electrocatalysts. *ACS Appl. Energy Mater.* **4**, 13819–13829 (2021).
38. Dai, Y. Q., Lu, P., Cao, Z. M., Campbell, C. T. & Xia, Y. N. The physical chemistry and materials science behind sinter-resistant catalysts. *Chem. Soc. Rev.* **47**, 4314–4331 (2018).
39. Challa, S. R. et al. Relating rates of catalyst sintering to the disappearance of individual nanoparticles during ostwald ripening. *J. Am. Chem. Soc.* **133**, 20672–20675 (2011).
40. Meier, J. C. et al. Design criteria for stable Pt/C fuel cell catalysts. *Beilstein J. Nanotechnol.* **5**, 44–67 (2014).
41. Yin, P. et al. Quantification of critical particle distance for mitigating catalyst sintering. *Nat. Commun.* **12**, 4865 (2021).
42. Swihart, D. L. & Mason, W. R. Electronic spectra of octahedral platinum(IV) complexes. *Inorg. Chem.* **9**, 1749–1757 (1970).
43. Shelimov, B., Lambert, J.-F., Che, M. & Didillon, B. Initial steps of the alumina-supported platinum catalyst preparation: a molecular study by 195Pt NMR, UV-Visible, EXAFS, and Raman spectroscopy. *J. Catal.* **185**, 462–478 (1999).
44. Jin, Z. S., Chen, Z. S., Li, Q. L., Xi, C. J. & Zheng, X. H. On the conditions and mechanism of PtO₂ formation in the photoinduced conversion of H₂PtCl₆. *J. Photochem. Photobiol., A* **81**, 177–182 (1994).
45. Gomez, S. et al. Platinum colloids stabilized by bifunctional ligands: self-organization and connection to gold. *Chem. Commun.* 1474–1475 (2001).
46. Hidai, S. et al. Platinum oxidation responsible for degradation of platinum–cobalt alloy cathode catalysts for polymer electrolyte fuel cells. *J. Power Sources* **215**, 233–239 (2012).
47. Han, B. H. et al. Record activity and stability of dealloyed bimetallic catalysts for proton exchange membrane fuel cells. *Energy Environ. Sci.* **8**, 258–266 (2015).
48. Wang, C. et al. Design and synthesis of bimetallic electrocatalyst with multilayered Pt-Skin Surfaces. *J. Am. Chem. Soc.* **133**, 14396–14403 (2011).
49. Escudero-Escribano, M. et al. Tuning the activity of Pt alloy electrocatalysts by means of the lanthanide contraction. *Science* **352**, 73–76 (2016).
50. Xie, M. et al. Pt–Co@Pt octahedral nanocrystals: enhancing their activity and durability toward oxygen reduction with an intermetallic core and an ultrathin shell. *J. Am. Chem. Soc.* **143**, 8509–8518 (2021).
51. Yarlagadda, V. et al. Boosting fuel cell performance with accessible carbon mesopores. *ACS Energy Lett.* **3**, 618–621 (2018).
52. Zhao, Z. P. et al. Tailoring a three-phase microenvironment for high-performance oxygen reduction reaction in proton exchange membrane fuel cells. *Matter* **3**, 1774–1790 (2020).
53. Nakaya, Y., Hirayama, J., Yamazoe, S., Shimizu, K.-I. & Furukawa, S. Single-atom Pt in intermetallics as an ultrastable and selective catalyst for propane dehydrogenation. *Nat. Commun.* **11**, 2838 (2020).
54. Chen, S. et al. Propane dehydrogenation on single-site [PtZn₄] intermetallic catalysts. *Chem.* **7**, 387–405 (2021).
55. Kabir, S. et al. Elucidating the dynamic nature of fuel cell electrodes as a function of conditioning: an ex situ material characterization and in situ electrochemical diagnostic study. *ACS Appl. Mater. Interfaces* **11**, 45016–45030 (2019).

Acknowledgements

We acknowledge the funding support from the National Key Research and Development Program of China (Grant 2018YFA0702001), the National Natural Science Foundation of China (Grants 22071225 and 51971211), the Plan for Anhui Major Provincial Science & Technology Project (Grants 202203a0520013 and 202103a05020015), the Fundamental Research Funds for the Central Universities (Grant WK2060190103), the Joint Funds from Hefei National Synchrotron Radiation Laboratory (Grant KY2060000175), the Collaborative Innovation Program of Hefei Science Center of CAS (Grant 2021HSC-CIP015), and Youth Innovation Promotion Association of CAS (Grant 2017483).

Author contributions

H.-W.L. and T.-W.S. conceived and designed the project. T.-W.S., C.X., Z.-T.S., H.-K.Y., L.T., W.-J.Z., and L.-J.Z. synthesized and characterized the catalysts. M.Z. performed the HAADF-STEM characterization. T.-W.S. and S.-Q.C. performed the X-ray absorption spectra measurements. P.C. performed the XPS test. T.-W.S., P.Y., and J.L. made the MEA. T.-W.S. and H.-W.L. co-wrote the manuscript. All the authors discussed the results and commented on the manuscript.

Competing interests

The authors declare no competing interests.

Additional information

Supplementary information The online version contains supplementary material available at <https://doi.org/10.1038/s41467-022-34037-7>.

Correspondence and requests for materials should be addressed to Hai-Wei Liang.

Peer review information *Nature Communications* thanks the anonymous reviewer(s) for their contribution to the peer review of this work.

Reprints and permissions information is available at <http://www.nature.com/reprints>

Publisher's note Springer Nature remains neutral with regard to jurisdictional claims in published maps and institutional affiliations.

Open Access This article is licensed under a Creative Commons Attribution 4.0 International License, which permits use, sharing, adaptation, distribution and reproduction in any medium or format, as long as you give appropriate credit to the original author(s) and the source, provide a link to the Creative Commons license, and indicate if changes were made. The images or other third party material in this article are included in the article's Creative Commons license, unless indicated otherwise in a credit line to the material. If material is not included in the article's Creative Commons license and your intended use is not permitted by statutory regulation or exceeds the permitted use, you will need to obtain permission directly from the copyright holder. To view a copy of this license, visit <http://creativecommons.org/licenses/by/4.0/>.

© The Author(s) 2022